SN 2017ens: THE METAMORPHOSIS OF A LUMINOUS BROADLINED TYPE IC SUPERNOVA INTO AN SN IIN

T.-W. Chen[1], C. Inserra[2], M. Fraser[3], T. J. Moriya[4], P. Schady[1], T. Schweyer[1], A. V. Filippenko[5,6], D. A. Perley[7], A. J. Ruiter[8,9], I. Seitenzahl[8,9], J. Sollerman[10], F. Taddia[10], J. P. Anderson[11], R. J. Foley[12], A. Jerkstrand[13], C.-C. Ngeow[14], Y.-C. Pan[12], A. Pastorello[15], S. Points[16], S. J. Smartt[17], K. W. Smith[17], S. Taubenberger[18,13], P. Wiseman[2], D. R. Young[17], S. Benetti[15], M. Berton[19,20], F. Bufano[21], P. Clark[17], M. Della Valle[22,23,24], L. Galbany[25], A. Gal-Yam[26], M. Gromadzki[27], C. P. Gutiérrez[2], A. Heinze[28], E. Kankare[17], C. D. Kilpatrick[12], H. Kuncarayakti[19,29], G. Leloudas[30], Z.-Y. Lin[14], K. Maguire[17], P. Mazzali[7], O. McBrien[17], S. J. Prentice[17], A. Rau[1], A. Rest[31,32], M. R. Siebert[12], B. Stalder[33], J. L. Tonry[28], and P.-C. Yu[14]

[1]Max-Planck-Institut für Extraterrestrische Physik, Giessenbachstraße 1, 85748, Garching, Germany; jchen@mpe.mpg.de

[2]Department of Physics and Astronomy, University of Southampton, Southampton, SO17 1BJ, UK

[3]School of Physics, O'Brien Centre for Science North, University College Dublin, Belfield, Dublin 4, Ireland

[4]Division of Theoretical Astronomy, National Astronomical Observatory of Japan, National Institutes for Natural Sciences, 2-21-1 Osawa, Mitaka, Tokyo 181-8588, Japan

[5]Department of Astronomy, University of California, Berkeley, CA 94720-3411, USA

[6]Miller Senior Fellow, Miller Institute for Basic Research in Science, University of California, Berkeley, CA 94720, USA

[7]Astrophysics Research Institute, Liverpool John Moores University, IC2, Liverpool Science Park, 146 Brownlow Hill, Liverpool L3 5RF, UK

[8]School of Physical, Environmental and Mathematical Sciences, University of New South Wales, Australian Defence Force Academy, Canberra, ACT 2600, Australia

[9]Research School of Astronomy and Astrophysics, Australian National University, Canberra, ACT 0200, Australia

[10]The Oskar Klein Centre, Department of Astronomy, AlbaNova, Stockholm University, SE-106 91 Stockholm, Sweden

[11]European Southern Observatory, Alonso de Córdova 3107, Casilla 19, Santiago, Chile

[12]Department of Astronomy and Astrophysics, University of California, Santa Cruz, CA 95064, USA

[13]Max-Planck Institut für Astrophysik, Karl-Schwarzschild Str. 1, D-85748 Garching, Germany

[14]Graduate Institute of Astronomy, National Central University, No. 300, Zhongda Rd., Zhongli Dist., Taoyuan City 32001, Taiwan

[15]INAF - Osservatorio Astronomico di Padova, Vicolo dell'Osservatorio 5, 35122 Padova, Italy

[16]CTIO/NOAO, Casilla 603, La Serena, Chile

[17]Astrophysics Research Centre, School of Mathematics and Physics, Queen's University Belfast, Belfast BT7 1NN, UK

[18]European Southern Observatory, Karl-Schwarzschild-Str. 2, 85748 Garching, Germany

[19]Finnish Centre for Astronomy with ESO (FINCA), FI-20014 University of Turku, Finland

[20]Aalto University Metsähovi Radio Observatory, Metsähovintie 114, FIN-02540 Kylmälä, Finland

[21]INAF - Osservatorio Astrofisico di Catania Via Santa Sofia, 78, 95123, Catania, Italy

[22]INAF - Osservatorio Astronomico di Napoli, Salita Moiariello, 16, I-80131, Napoli, Italy

[23]Instituto de Astrofisica de Andalucia (IAA-CSIC), Glorieta de la Astronomia s/n, E-18008 Granada, Spain

[24]International Center for Relativistic Astrophysics, Piazza della Repubblica 10, I-65122 Pescara, Italy

[25]PITT PACC, Department of Physics and Astronomy, University of Pittsburgh, Pittsburgh, PA 15260, USA

[26]Department of Particle Physics and Astrophysics, Weizmann Institute of Science, Rehovot 76100, Israel

[27]Warsaw University Astronomical Observatory, Al. Ujazdowskie 4, 00-478 Warszawa, Poland

[28]Institute for Astronomy, University of Hawaii, 2680 Woodlawn Drive, Honolulu, HI 96822, USA

[29]Tuorla Observatory, Department of Physics and Astronomy, FI-20014 University of Turku, Finland

[30]DTU Space, National Space Institute, Technical University of Denmark, Elektrovej 327, 2800 Kgs. Lyngby, Denmark

[31]Space Telescope Science Institute, 3700 San Martin Drive, Baltimore, MD 21218, USA

[32]Department of Physics and Astronomy, Johns Hopkins University, Baltimore, MD 21218, USA

[33]LSST, 950 N. Cherry Ave, Tucson, AZ 85719

ABSTRACT

We present observations of supernova (SN) 2017ens, discovered by the ATLAS survey and identified as a hot blue object through the GREAT program. The redshift $z = 0.1086$ implies a peak brightness of $M_g = -21.1$ mag, placing the object within the regime of superluminous supernovae. We observe

a dramatic spectral evolution, from initially being blue and featureless, to later developing features similar to those of the broadlined Type Ic SN 1998bw, and finally showing $\sim 2000\,\mathrm{km\,s^{-1}}$ wide Hα and Hβ emission. Relatively narrow Balmer emission (reminiscent of a SN IIn) is present at all times. We also detect coronal lines, indicative of a dense circumstellar medium. We constrain the progenitor wind velocity to ~ 50–$60\,\mathrm{km\,s^{-1}}$ based on P-Cygni profiles, which is far slower than those present in Wolf-Rayet stars. This may suggest that the progenitor passed through a luminous blue variable phase, or that the wind is instead from a binary companion red supergiant star. At late times we see the $\sim 2000\,\mathrm{km\,s^{-1}}$ wide Hα emission persisting at high luminosity ($\sim 3 \times 10^{40}\,\mathrm{erg\,s^{-1}}$) for at least 100 day, perhaps indicative of additional mass loss at high velocities that could have been ejected by a pulsational pair instability.

1. INTRODUCTION

Type Ic supernovae (SNe) arise from the core collapse of a massive star that has lost its hydrogen and helium layers prior to exploding, through either strong stellar winds or interaction with a binary companion (e.g., Filippenko 1997; Gal-Yam 2017). Their light curves are powered by the radioactive decay of ^{56}Ni that is produced in the SN explosion. Related to these events, but with luminosities up to 100 times higher, are the Type I superluminous SNe (SLSNe I; see Gal-Yam 2012; Inserra et al. 2018a; Moriya et al. 2018b for reviews of observations and models). SLSNe exhibit spectral similarities to SNe Ic (Pastorello et al. 2010), but their luminosities are such that they cannot be powered solely by radioactive decay (Quimby et al. 2011). The nature of the additional energy source remains unknown, with suggestions ranging from a central engine (Kasen & Bildsten 2010; Woosley 2010) to interaction with a massive H and He-free circumstellar medium (CSM; Chevalier & Irwin 2011).

Some SNe Ib/Ic have been observed to develop relatively narrow ($\sim 500-1000\,\mathrm{km\,s^{-1}}$) emission lines of hydrogen in their spectra; examples include SNe Ib 2014C and 2004dk (Milisavljevic et al. 2015; Mauerhan et al. 2018) and SNe Ic 2001em and 2017dio (Gal-Yam 2017; Kuncarayakti et al. 2018). This has been interpreted as evidence that for at least some H-poor SNe, the fast ejecta are colliding with H-rich material relatively far from the star. This late-time interaction has also been observed in some SLSNe Ic which show Hα emission at $+70$ to $+250\,\mathrm{d}$ after their peak brightness (Yan et al. 2015, 2017).

In this Letter we report on the discovery of an unusual SN with our GREAT (**GR**OND-e**PESSTO-AT**LAS; Greiner et al. 2008; Smartt et al. 2015; Tonry et al. 2018) Survey. We introduce this program here, which is designed to rapidly identify hot, blue transients, with the specific goal of finding very young SLSNe in faint galaxies (Chen et al. 2017b). SN 2017ens (ATLAS17gqa) was discovered by the ATLAS survey on 2017 June 5 (UT dates are used herein), located at (J2000) $\alpha = 12^h04^m09^s.37$, $\delta = -01°55'52.2''$. Prompted by the high blackbody temperature of $21,000 \pm 3000\,\mathrm{K}$ that we measured with our

GREAT data on 2017 June 8 (Chen et al. 2017a), we began an intensive spectroscopic and photometric follow-up campaign (Sec. 2).

The adopted redshift of SN 2017ens, $z = 0.1086$ (Sec. 3.3), implies an absolute magnitude of $M_g = -21.1$ at peak, and thus a luminosity consistent with a SLSN (Gal-Yam 2012). In Sec. 3 we present the spectral evolution of SN 2017ens, which began to show $\sim 2000\,\mathrm{km\,s^{-1}}$ wide Hα and Hβ emission after $+163\,\mathrm{d}$ (phases are corrected for time dilation and are relative to the GROND r-band maximum on MJD $= 57{,}924.011$). We compare the spectral properties of SN 2017ens to those of other SLSNe and broadlined SNe Ic (SNe Ic-BL), and also present the detections of rarely seen coronal lines. The bolometric light curve and modeling results are described in Sec. 4. Finally, in Sec. 5 we discuss plausible scenarios that may explain the spectral evolution and luminosity of SN 2017ens. We adopt a cosmology of $H_0 = 72$ km s^{-1} Mpc^{-1}, $\Omega_\Lambda = 0.73$, and $\Omega_m = 0.27$. The foreground reddening toward SN 2017ens is $A_V = 0.058\,\mathrm{mag}$ (Schlafly & Finkbeiner 2011), and we assume that host-galaxy extinction is negligible because no Na I D absorption is visible in the SN spectrum.

2. OBSERVATIONS

Our photometric coverage of SN 2017ens spans the ultraviolet (UV) with the Ultraviolet and Optical Telescope (UVOT) on the Neil Gehrels *Swift* Observatory, optical wavelengths with GROND, ATLAS, LCO 1 m[1], and Lulin Super Light Telescope (SLT)[2], and near-infrared (NIR) bands with GROND. We use standard procedures to reduce the data (Poole et al. 2008 for UVOT; Krühler et al. 2008 for GROND). Ground-based optical photometry is calibrated against the Sloan Digital Sky Survey (SDSS). For ATLAS magnitudes we apply passband corrections using spectra (prescription from Inserra et al. 2018b); for SLT data we use the conversion of R. Lupton[3]. The NIR magnitudes are calibrated against Two Micron All Sky Survey (2MASS) field stars. All data are reported in the AB system, and errors include the statistical and systematic uncertainties. We do not have host-galaxy templates,

but we estimate a $< 15\%$ contribution from host light ($r > 23$ mag measured in pre-explosion Panoramic Survey Telescope and Rapid Response System (PanSTARRS) images) to our SN photometry after $+150$ d. Our photometric results are given in a machine-readable table and shown in Fig. 1 (top panel).

We obtained a series of spectra of SN 2017ens, following the SN evolution from $+4$ d to $+265$ d (log of observations in Table 1). Spectra are reduced in the standard fashion (ALFOSCGUI pipeline[4] for ALFOSC) or using custom-built pipelines PyWiFeS (Childress et al. 2014) for WiFeS, LPipe[5] for LRIS, Krühler et al. (2015) for X-Shooter, and Smartt et al. (2015) for EFOSC2. Finally, we correct the spectral-flux calibration against r-band photometry. The resulting calibration error estimated by comparing to g-band photometry is generally < 0.10 mag, with the exception of the WiFeS (0.15 mag) and Keck (0.25 mag) spectra. (Those data were taken at very high airmass, making flux calibration difficult.) All spectra will be available through WISeREP (Yaron & Gal-Yam 2012).

3. ANALYSIS AND RESULTS

3.1. *Light Curves and Comparison*

The discovery epoch of SN 2017ens with $M_r \approx -19.8$ mag is at MJD = 57,909.3. ATLAS monitored the field daily for 23 d before discovery. From a deep image taken 3 d before discovery ($M_r \approx -18.7$ mag), we constrain the explosion date of SN 2017ens to MJD = $57,907.8 \pm 1.5$; thus, the rest-frame rise time is ~ 15 d.

Fig. 1 (middle panel) shows the absolute g-band light curve, which we compare to SLSNe, SNe IIn, and SNe Ic-BL selected based on the photometric properties and spectral evolution (see Sec. 3.2) of SN 2017ens. At peak, SN 2017ens is ~ 10 times more luminous than the SNe Ic-BL 1998bw (Patat et al. 2001), 2003jd (Valenti et al. 2008), and SN Ic 2017dio (Kuncarayakti et al. 2018), which shows narrow H and He emission in its spectra. The early-phase light-curve evolution of SN 2017ens is similar to that of rapidly evolving SLSNe such as LSQ14mo (Chen et al. 2017c; Leloudas et al. 2015) and SN 2010gx (Pastorello et al. 2010). SN 2017ens shows no sign of undulations in its light curves, as are often observed in slowly evolving SLSNe as well as SLSNe that exhibit late-time Hα such as iPTF13ehe (Yan et al. 2015) and iPTF15esb (Yan et al. 2017). At late times, the light curves of SN 2017ens remain approximately constant, indicating that strong interaction dominates, as in SN IIn 2010jl before $+300$ d (Fransson et al. 2014).
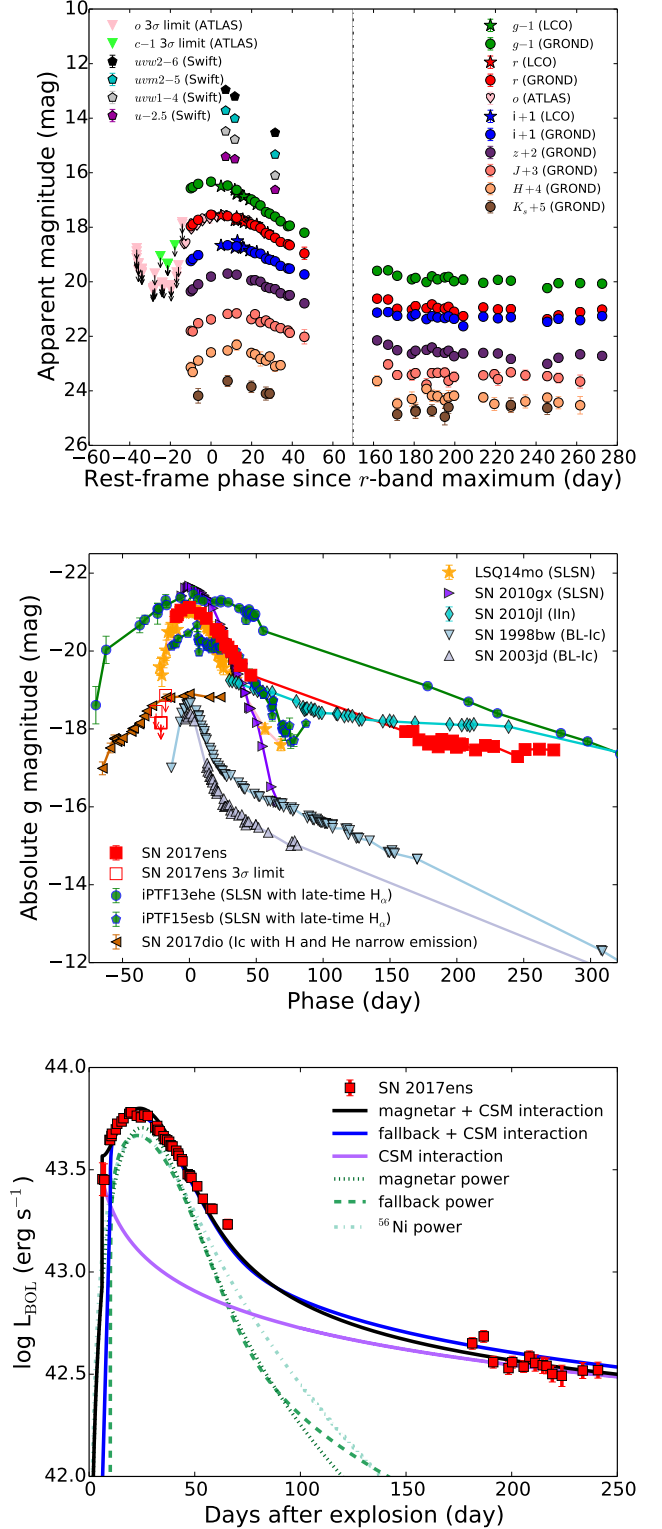
Figure 1: *Top panel:* multiband light curves of SN 2017ens. Note the discontinuous abscissa. *Middle panel:* light-curve comparison in absolute g band with the SNe chosen for spectroscopic comparison. *Bottom panel:* bolometric light curve of SN 2017ens and model fitting.

3.2. *Spectroscopic Evolution and Comparison*

We show the spectral evolution of SN 2017ens in Fig. 2. Around maximum light the spectra are blue and featureless. In the first spectrum taken at $+4$ d after peak, we detect narrow Hα and Hβ emission lines (barely resolved width of $\sim 100\,\mathrm{km\,s^{-1}}$). Fitting the dereddened spectra with a blackbody gives a temperature of $T_{\mathrm{BB}} \geq 10,300\,\mathrm{K}$, consistent with our estimate from the GROND analysis ($\geq 11,500\,\mathrm{K}$). At ~ 1 month after peak, some broad features emerge, similar to those seen in SNe Ic-BL after peak brightness (e.g., Patat et al. 2001). Apart from narrow Hα and Hβ, we detect a narrow He I $\lambda 5876$ emission line. The commonly observed [O II], [O III], and [N II] host-galaxy emission lines are absent, suggesting that the observed Balmer lines originate from the transient itself, not the underlying host (Perley et al. 2017). We also check the WiFeS datacubes and see no [O III] emission at the SN position.

At late times (> 160 d) after the SN emerged from solar conjunction, our data reveal dramatic evolution, with the spectra more resembling those of SNe IIn. The spectra are still blue, but now dominated by prominent, $\sim 2000\,\mathrm{km\,s^{-1}}$ wide Balmer emission lines, indicative of much stronger interaction with H-rich CSM. The luminosity and the velocity of the $\sim 2000\,\mathrm{km\,s^{-1}}$ Hα line does not vary significantly between $+163$ and $+264$ d, staying at $\sim 3 \times 10^{40}\,\mathrm{erg\,s^{-1}}$.

The spectral evolution of SN 2017ens is unique, sharing features with several distinct SN subclasses (Fig. 3 top panel). In the earliest phases, the blue and featureless spectra share a similarity with young core-collapse SN spectra. We do not see the O II absorption features commonly associated with SLSNe. However, we may have missed them in SN 2017ens. For example, SLSN 2010gx (Pastorello et al. 2010) displayed O II absorption before it peaked and then became blue and featureless.

As the spectra evolve, SN 2017ens is not well matched to other SLSNe such as LSQ14mo (Chen et al. 2017c) and iPTF15esb (Yan et al. 2017). Rather, it appears to be more similar to SNe Ic-BL. The classification tool GELATO (Harutyunyan et al. 2008) applied to the SN 2017ens $+27$ d spectrum returns the closest similarity with SN 1998bw at $+22$ d (Patat et al. 2001) and SN 2003jd at -0.3 d (Modjaz et al. 2014). These two SNe Ic-BL still provide a good match to SN 2017ens when we remove the continua assuming a blackbody (Fig. 3, middle panel). SN 2017ens has a somewhat bluer continuum, perhaps due to CSM interaction, as was the case for SN 2017dio at $+6$ d (Kuncarayakti et al. 2018). The origin of the broad feature around $6530\,\text{Å}$ is uncertain; it could be attributed to a blend of Si and Fe/Co lines, Hα associated with interaction, or the C II $\lambda 6580$ line sometimes seen in SLSNe (e.g., SN 2018bsz; Anderson et al. 2018).

During the late-time strongly interacting phase, the overall spectral features of SN 2017ens are well matched with those of SN 2017dio at $+83$ d. Both SNe exhibit a blue pseudocontinuum (below $\sim 5000\,\text{Å}$) that is more significant than in iPTF13ehe at $+251$ d (Yan et al. 2015); it is likely produced by Fe II lines (Smith et al. 2009).

3.3. *Nebular and Coronal Lines*

The VLT/X-Shooter spectra around $+190$ d (Fig. 4) provide higher resolution and wider wavelength coverage than our other spectra, enabling us to detect many narrow emission lines. Interestingly, we find that the flux ratio of the nebular [O III] $\lambda\lambda 4959, 5007$ and auroral [O III] $\lambda 4363$ lines is 0.45, consistent with coronal lines that may arise from X-ray photoionization (Fransson et al. 2002) of dense gas (see Filippenko & Halpern 1984, their Fig. 11). Therefore, we conclude that the [O III] $\lambda 4363$ line comes from the SN, and we use it to constrain the redshift of SN 2017ens to $z = 0.1086$, consistent with the average of the [O II] $\lambda 3727$ and [O III] $\lambda\lambda 4959, 5007$ lines.

These narrow coronal lines have been seen in only a handful of SNe IIn and the transitional object SN 2011hw (Pastorello et al. 2015). The ratio [O III]$\lambda 4363$/[O III]$\lambda\lambda 4959, 5007$ for SN 2017ens is similar to that seen in SN 2005ip at $+173$ d (Smith et al. 2009), SN 2006jd at $+1542$ d (Stritzinger et al. 2012), and SN 2010jl at $+461$ d and $+573$ d (Fransson et al. 2014). Other coronal lines detected in SN 2017ens are similar to those seen in SN 2010jl (Fig. 3, bottom panel): [Fe X] $\lambda 6374.5$ is strong, as are [Fe XI] $\lambda 7891.8$, [Ne V] $\lambda\lambda 3345.8$, 3425.9, [Ca V] $\lambda 6086.8$, and [Ar X] $\lambda 5533.2$. The presence of these lines is indicative of a highly ionized and dense CSM, although we do not detect the highest-ionization coronal lines such as [Fe XIV] $\lambda 5302.9$ and [Ar XIV] $\lambda 4412.3$, which were seen in SN 2005ip.

The flux ratio of the [O III] $\lambda 4363$ to $\lambda 5007$ lines is a function of the CSM density and temperature. Following Fransson et al. (2014, their Fig. 26), we use our measured flux ratio, $\log(\lambda 4363/\lambda 5007) = -0.22$, to constrain the CSM electron density to lie between 10^6 and $10^8\,\mathrm{cm^{-3}}$ for $T_e = 50,000$ to $10,000\,\mathrm{K}$. This density range is consistent with that observed for SN 2010jl.

From our mid-resolution X-Shooter data, we resolve narrow P-Cygni profiles on top of the $\sim 2000\,\mathrm{km\,s^{-1}}$ wide Balmer and Paschen lines. We measure the blueshifted wavelength from the absorption component of the Hγ, Hβ, and Hα P-Cygni profiles, which suggests that the unshocked CSM has a low velocity of $\sim 50\,\mathrm{km\,s^{-1}}$. A similar velocity of $\sim 60\,\mathrm{km\,s^{-1}}$ is obtained from the P-Cygni profile of the He I $\lambda 10,830$ line. Moreover, we measure the full width at half-maximum intensity (FWHM) of the wide components, such as Hα ($2500 \pm 700\,\mathrm{km\,s^{-1}}$), H$\beta$ ($2300 \pm 400\,\mathrm{km\,s^{-1}}$), Pa$\gamma$ ($2000 \pm 200\,\mathrm{km\,s^{-1}}$), and He I
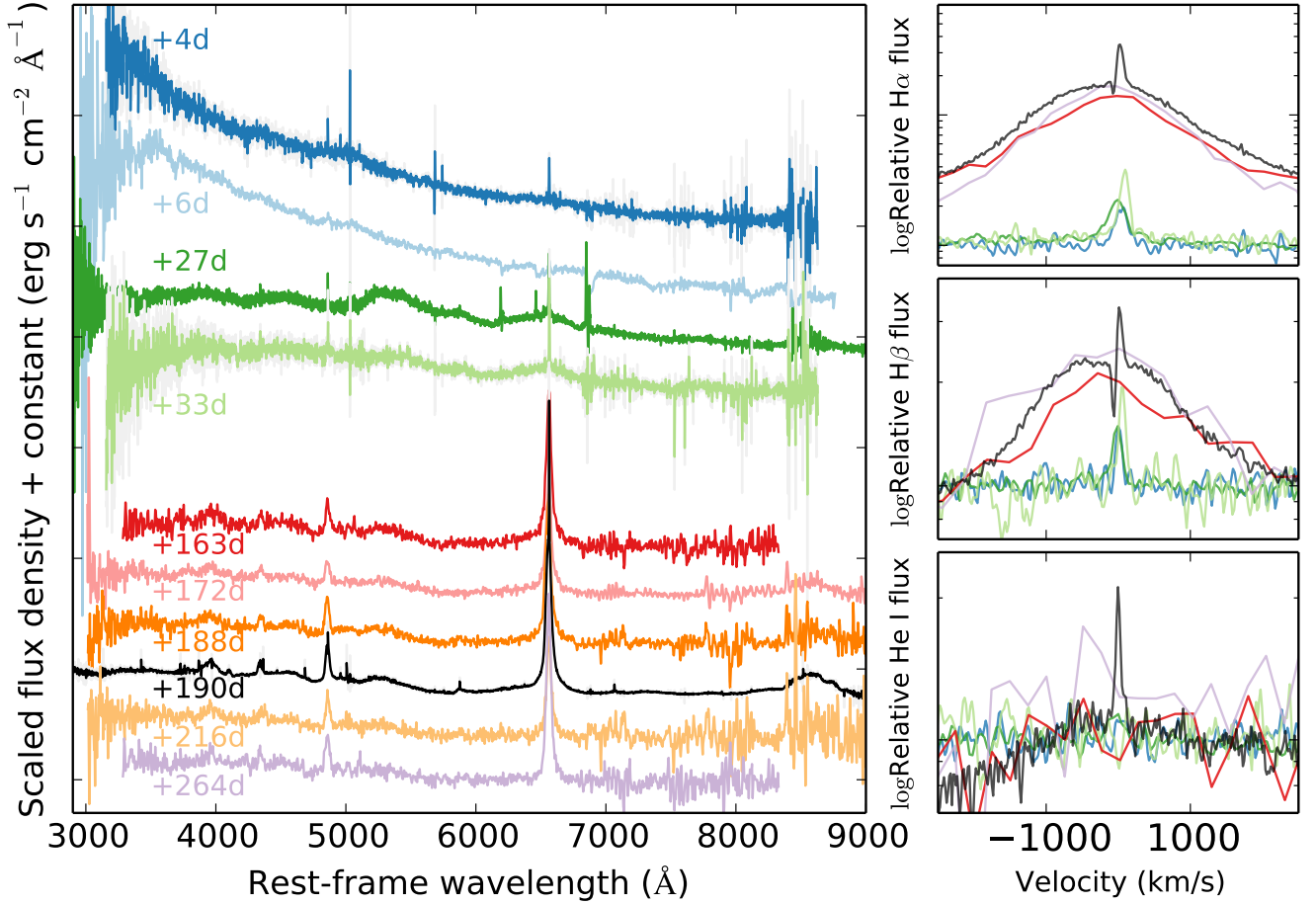
Figure 2: Spectroscopic evolution of SN 2017ens. The right panels show the velocity of the Hα, Hβ, and He I λ5876 lines at selected epochs. Each phase is shown with the same color as in the main panel.

λ10, 830 (2200 $\pm$ 200 km s^{-1}). We also detect narrow absorption lines from the Balmer series (no clear emission), spanning Hϵ to H33 (3659 Å).

In addition, we see emission from the H II region close to the host-galaxy center (see Fig. 4, marked B1), as part of a faint galaxy (SDSS J120409.47−015552.4) with $g = 21.92 \pm 0.24$ mag ($M_g \approx -16.5$ mag). These lines have a slightly different redshift ($z = 0.1084$) than SN 2017ens. In particular, the (noisy) detection of the weak auroral [O III] λ4363 line indicates a low host-galaxy metallicity of ~ 0.04–$0.4 Z_\odot$ using the direct T$_e$-based method. If we instead use the empirical N2 metallicity diagnostic (Pettini & Pagel 2004), we measure $Z = 0.3 \pm 0.2 Z_\odot$.

## 4. BOLOMETRIC LIGHT CURVE AND MODEL FITTING

Using all of our available UV-through-NIR photometry, we built a pseudobolometric light curve for SN 2017ens using the prescription from Inserra et al. (2018b). The results are very similar to those derived when using a blackbody fit, as expected as our photometry covers a large wavelength range. From a polynomial fit to the bolometric data we obtain $L_{\mathrm{bol}} = (5.86 \pm 0.20) \times 10^{43}$ erg s^{-1} at peak and an integrated energy of $(3.53 \pm 1.42) \times 10^{50}$ erg.

To fit our bolometric light curve, we used a two-component model consisting of a central heating and an interaction component. First, the centrally heated component uses the standard Arnett method (Arnett 1982; Inserra et al. 2013). We tested three possible central power sources: the nuclear decay of ^{56}Ni, the spindown of a magnetar (Kasen & Bildsten 2010), and fallback accretion (Dexter & Kasen 2013; Moriya et al. 2018a). The ^{56}Ni decay and the magnetar spindown light curves are obtained as by Inserra et al. (2013), but the magnetar model takes the gamma-ray opacity from the magnetar into account as by Chen et al. (2015). The fallback accretion power is obtained by assuming a central energy input of $L_{\mathrm{fallback},1}(t/1\,\mathrm{s})^{-5/3}$, where $L_{\mathrm{fallback},1}$ is a constant (Dexter & Kasen 2013). Second, for the interaction component,
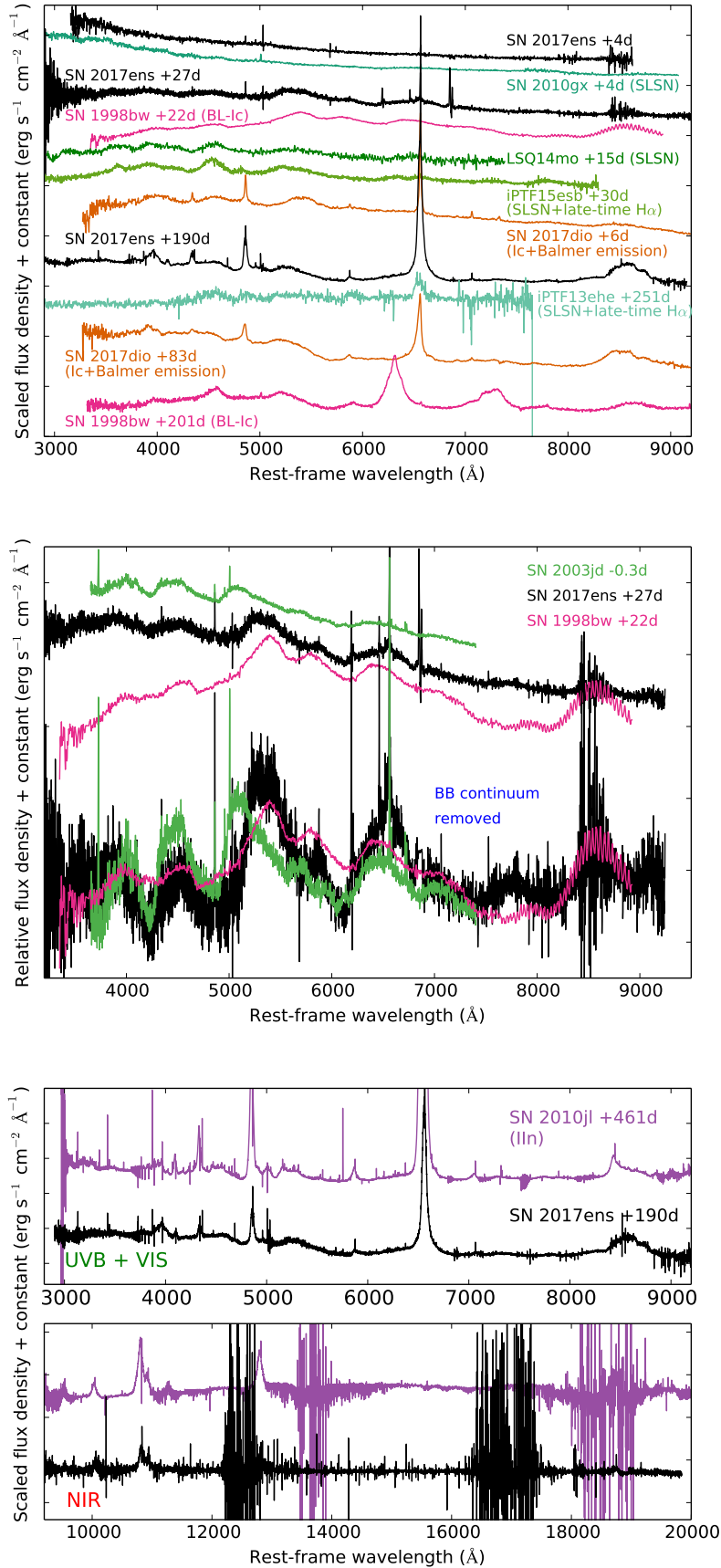
Figure 3: *Top panel:* comparison between SN 2017ens and other SNe at three selected epochs. *Middle panel:* comparison between SN 2017ens and the Type Ic-BL SNe 1998bw and 2003jd. The lower spectra have their continuum removed assuming a blackbody. *Bottom panel:* comparison between SN 2017ens and the Type IIn SN 2010jl at optical and NIR wavelengths.
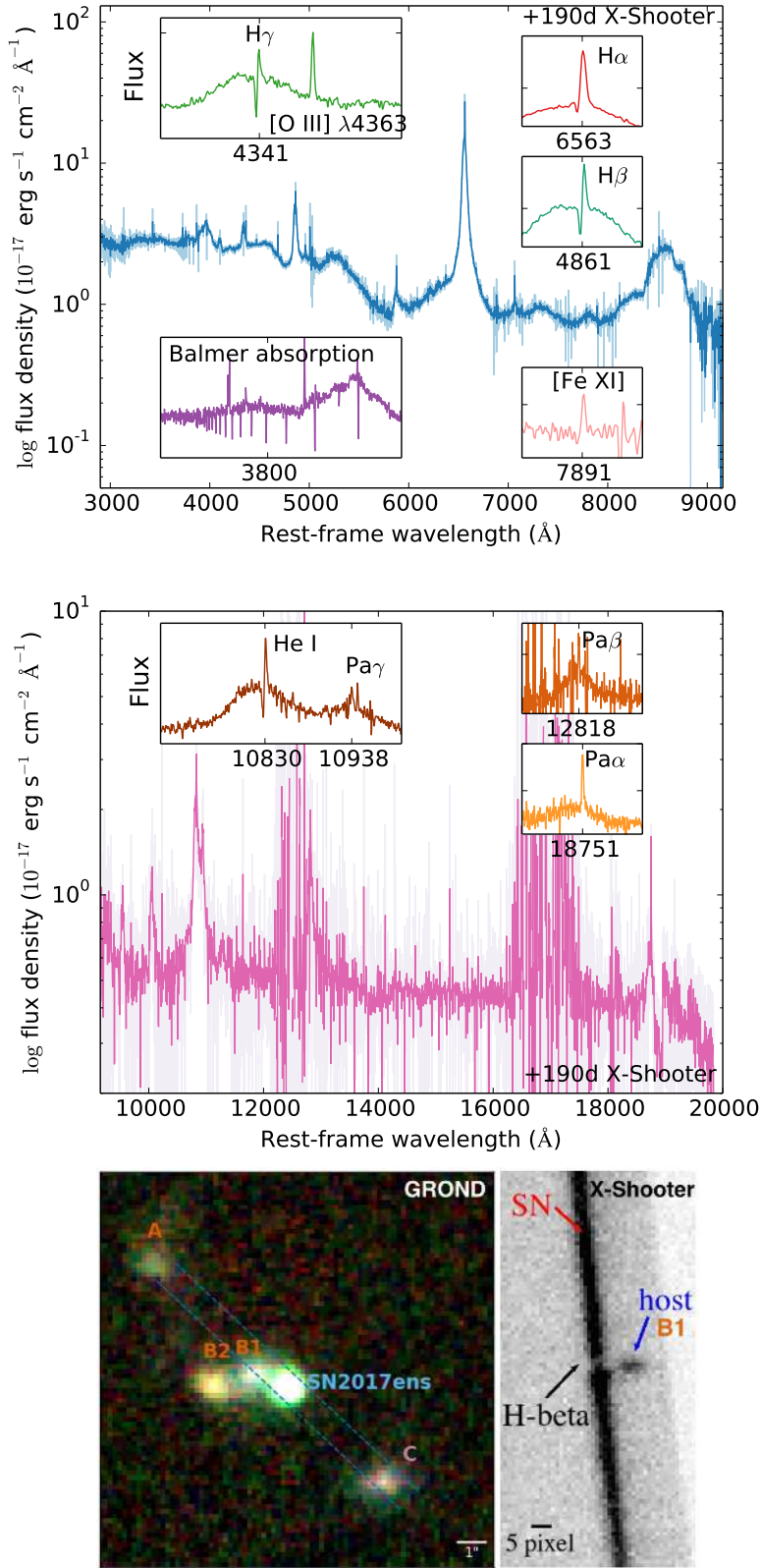
Figure 4: VLT/X-Shooter spectra of SN 2017ens at +190 d. *Top panel:* UVB and optical (VIS) parts. *Middle panel:* NIR part. The main panels use a log scale in order to present details in the continuum (rebinned to 2 Å pixel^{-1} (UVB+VIS) and 5 Å pixel^{-1} (NIR)); inset panels use a linear scale without binning. *Bottom panel left:* color-combined image from GROND $r'i'z'$ bands. SN 2017ens is associated with host-galaxy B1+B2, and there is a possible tidal tail connecting to the nearby object A (redshift unknown). Source C is a background galaxy at $z = 0.30$. The X-Shooter slit position is indicated with two dashed lines. *Bottom panel right:* the Hβ position in the two-dimensional raw image.

we adopted a steady-wind CSM, and the input luminosity from this component goes as $L_{\mathrm{int},1}(t/1\,\mathrm{s})^{-3/5}$, where the outer SN density structure is proportional to r^{-7} (Moriya et al. 2013). The inner SN density structure is assumed to be constant.

We first used the interaction component to fit the bolometric light curve 150 d after explosion, assuming that interaction is the dominant light source at this time. We then derived the contribution required from a central power source at early times to provide a good light-curve match. Given that the spectra of SN 2017ens and SN 1998bw are similar (Fig. 3), we used the relation $(E_{\mathrm{ej}}/10^{51}\,\mathrm{erg})/(M_{\mathrm{ej}}/M_{\odot}) \approx 3$ found for SN 1998bw (Nakamura et al. 2001) to break the degeneracy between E_{ej} and M_{ej}.

Fig. 1 (bottom panel) shows the results of our fits. In all cases, the CSM interaction model that we used has $L_{\mathrm{int},1} = 7.7 \times 10^{46}\,\mathrm{erg\,s^{-1}}$. The inner edge of the CSM is set at $1.2 \times 10^{15}\,\mathrm{cm}$ to match the early light-curve rise in the model, but this constraint is not strong. We find that all three centrally heated models provide reasonable fits to the bolometric light curve. They all have $E_{\mathrm{ej}} = 1.5 \times 10^{52}\,\mathrm{erg}$ and an ejecta mass of $5\,M_{\odot}$. However, the $^{56}\mathrm{Ni}$-powered light curve requires a very high $^{56}\mathrm{Ni}$ mass of $3.5\,M_{\odot}$. This is close to the ejecta mass, and we therefore find the $^{56}\mathrm{Ni}$-powered model to be unlikely. Alternatively, a magnetar central engine with an initial spin of $3.8\,\mathrm{ms}$ and a magnetic field of $8 \times 10^{13}\,\mathrm{G}$, and fallback accretion with $L_{\mathrm{fallback},1} = 6 \times 10^{53}\,\mathrm{erg\,s^{-1}}$, provide good qualitative fits to the light curve. It is of course possible that the entire light curve is driven by different degrees of interaction. The contribution of the interaction component at early times (0–70 d after explosion) is $\sim 20\%$, while it is $\gtrsim 90\%$ at late times (200 d).

Assuming the above best-fit results and a kinetic energy to radiation conversion efficiency at the shock of 0.1 (Moriya et al. 2013), we estimate the mass-loss rate of the progenitor to be $5 \times 10^{-4}\,M_{\odot}\,\mathrm{yr^{-1}}$, with a constant wind velocity of $50\,\mathrm{km\,s^{-1}}$. The CSM density estimate is similar to those of SNe IIn showing similar coronal lines (Taddia et al. 2013).

5. DISCUSSION

One important clue to interpreting the possible powering mechanisms behind SN 2017ens is that we measured the H-rich material to have a velocity of ~ 50–$60\,\mathrm{km\,s^{-1}}$ from the blueshifted absorption of the narrow P-Cygni profiles. This wind velocity is far slower than those present in Wolf-Rayet star winds. If this wind is from the progenitor, it could come from a massive H-rich progenitor (such as a luminous blue variable) that explosively ejected its H envelope shortly before the SN explosion. Alternatively, this wind could come from a pulsational pair-instability SN with a slow and long-term stable wind (Woosley 2017).

It is also possible that SN 2017ens exploded as a SN Ic-BL inside a patchy, H-rich CSM from a binary companion; the expanding ejecta interact with the bulk of the CSM at later times, as has been suggested for SN 2017dio (Kuncarayakti et al. 2018). Alternatively, as proposed for ASASSN-15no (Benetti et al. 2018), a dense inner CSM may have hidden the SN features at early times, before they become briefly visible as the CSM was swept up by the ejecta. At late times they could have again been masked by an increasingly strong interaction component. A special CSM geometry (e.g., doughnut shape) is also probable, and we see the SN Ic-BL along a certain viewing angle.

In the case of a binary companion, the wind of ~ 50–$60\,\mathrm{km\,s^{-1}}$ and mass-loss rate of $5 \times 10^{-4}\,M_{\odot}\,\mathrm{yr^{-1}}$ are consistent with a red supergiant (Goldman et al. 2017), albeit at the more extreme end, which can be explained by the companion having gained mass from the SN progenitor during an earlier accretion phase. If so, this may suggest that the progenitor of SN 2017ens lost its H and He layers through interaction with a binary companion.

We must also consider the apparent $\sim 2000\,\mathrm{km\,s^{-1}}$ material given its high luminosity. If this is associated with mass loss from the progenitor, and the line width is not from electron scattering as seen in many SNe IIn, then the material is moving much faster than the winds of H-rich stars (or the CSM of SNe IIn). It is difficult to imagine how this could be produced by anything other than a sudden ejection of the H envelope, shortly before the SN explosion. In fact, the luminosity of the $\sim 2000\,\mathrm{km\,s^{-1}}$ wide component of Hα is comparable to that seen in SN 1995N (Fransson et al. 2002) ($\sim 2.3 \times 10^{40}\,\mathrm{erg\,s^{-1}}$), and it may be too large to be coming solely from swept-up material. A pulsational pair-instability explosion is at least qualitatively consistent with an outburst that can unbind the H envelope shortly before an SN explosion. This scenario is also consistent with the measured low-metallicity environment.

The unique spectroscopic evolution of SN 2017ens together with its high luminosity poses challenges to all currently known SN scenarios. While detailed modeling can help elucidate the nature of this transient, ongoing surveys for SLSNe such as GREAT will find more such peculiar transients. With a larger sample and high-cadence follow-up spectroscopy, we will be able to further understand the nature of SN 2017ens-like objects and the role of interaction in SLSNe.

Table 1: Log of spectroscopic observations of SN 2017ens and its host galaxy.

UT Date	MJD	Phase (day)	Telescope	Instrument	Grating/Grism /Arm	Exp. Time (s)	Slit ('')	Resolution (Å)	Range (Å)
2017 Jun. 24	57928.392	3.95	ANU 2.3 m	WiFeS[a]	B3000/R3000	1200/1200	IFU	1.6/2.5	3500–5700/5400–9500
2017 Jun. 26	57930.356	5.72	NOT	ALFOSC	Gr#4	1800	1.0	16	3300–9700
2017 Jul. 20	57954.264	27.29	Keck I	LRIS	B600/R400	1125	0.7	5/6	3200–10,000
2017 Jul. 26	57960.356	32.78	ANU 2.3 m	WiFeS[a]	B3000/R3000	1200/1200	IFU	1.6/2.5	3500–5700/5400–9500
2017 Dec. 17	58104.325	162.65	NTT	EFOSC2	Gr#13	2700	1.0	18.2	3700–9200
2017 Dec. 27	58114.301	171.65	NTT	EFOSC2	Gr#11/Gr#16	2700/2700	1.0/1.0	13.8/13.4	3400–7400/6000–9900
2018 Jan. 14	58132.275	187.86	VLT	X-Shooter	UVB/VIS/NIR	3600/3400/3680	0.9/0.9/1.0	1/1.1/3.3	3000–5560/5450–10,200/10,000–20,600
2018 Jan. 14	58132.312	187.90	NTT	EFOSC2	Gr#11	3600	1.0	13.8	3400–7400
2018 Jan. 15	58133.263	188.75	VLT	X-Shooter	UVB/VIS/NIR	7200/6800/7360	0.9/0.9/1.0	1/1.1/3.3	3000–5560/5450–10,200/10,000–20,600
2018 Jan. 15	58133.273	188.76	NTT	EFOSC2	Gr#16	2700	1.0	13.4	6000–9900
2018 Jan. 16	58134.268	189.66	VLT	X-Shooter	UVB/VIS/NIR	3600/3400/3680	0.9/0.9/1.0	1/1.1/3.3	3000–5560/5450–10,200/10,000–20,600
2018 Jan. 19	58137.305	192.40	VLT	X-Shooter	UVB/VIS/NIR	3600/3400/3680	0.9/0.9/1.0	1/1.1/3.3	3000–5560/5450–10,200/10,000–20,600
2018 Feb. 14	58163.277	215.83	NTT	EFOSC2	Gr#11	8100	1.0	13.8	3400–7400
2018 Feb. 18	58167.245	219.41	NTT	EFOSC2	Gr#16	5400	1.0	13.4	6000–9900
2018 Apr. 9	58217.065	264.35	NTT	EFOSC2	Gr#13	2700	1.0	18.2	3650–9200

[a] WiFeS is an integral field unit (IFU) with 25 slitlets that are 1'' wide and 38'' long. Resolution is measured from the night-sky lines.

REFERENCES

Anderson, J. P., Pessi, P. J., Dessart, L., et al. 2018, ArXiv e-prints, arXiv:1806.10609

Arnett, W. D. 1982, ApJ, 253, 785

Benetti, S., Zampieri, L., Pastorello, A., et al. 2018, MNRAS, 476, 261

Chen, T.-W., Smartt, S. J., Jerkstrand, A., et al. 2015, MNRAS, 452, 1567

Chen, T.-W., Inserra, C., Smartt, S. J., et al. 2017a, The Astronomer's Telegram, 10478

Chen, T.-W., Schady, P., Kruehler, T., et al. 2017b, The Astronomer's Telegram, 10510

Chen, T.-W., Nicholl, M., Smartt, S. J., et al. 2017c, A&A, 602, A9

Chevalier, R. A., & Irwin, C. M. 2011, ApJL, 729, L6

Childress, M. J., Vogt, F. P. A., Nielsen, J., & Sharp, R. G. 2014, Ap&SS, 349, 617

Dexter, J., & Kasen, D. 2013, ApJ, 772, 30

Filippenko, A. V. 1997, ARA&A, 35, 309

Filippenko, A. V., & Halpern, J. P. 1984, ApJ, 285, 458

Fransson, C., Chevalier, R. A., Filippenko, A. V., et al. 2002, ApJ, 572, 350

Fransson, C., Ergon, M., Challis, P. J., et al. 2014, ApJ, 797, 118

Gal-Yam, A. 2012, Science, 337, 927

—. 2017, Observational and Physical Classification of Supernovae, ed. A. W. Alsabti & P. Murdin, 195

Goldman, S. R., van Loon, J. T., Zijlstra, A. A., et al. 2017, MNRAS, 465, 403

Greiner, J., Bornemann, W., Clemens, C., et al. 2008, PASP, 120, 405

Harutyunyan, A. H., Pfahler, P., Pastorello, A., et al. 2008, A&A, 488, 383

Inserra, C., Prajs, S., Gutierrez, C. P., et al. 2018a, ApJ, 854, 175

Inserra, C., Smartt, S. J., Jerkstrand, A., et al. 2013, ApJ, 770, 128

Inserra, C., Smartt, S. J., Gall, E. E. E., et al. 2018b, MNRAS, 475, 1046

Kasen, D., & Bildsten, L. 2010, ApJ, 717, 245

Krühler, T., Küpcü Yoldaş, A., Greiner, J., et al. 2008, ApJ, 685, 376

Krühler, T., Malesani, D., Fynbo, J. P. U., et al. 2015, A&A, 581, A125

Kuncarayakti, H., Maeda, K., Ashall, C. J., et al. 2018, ApJL, 854, L14

Leloudas, G., Patat, F., Maund, J. R., et al. 2015, ApJL, 815, L10

Mauerhan, J. C., Filippenko, A. V., Zheng, W., et al. 2018, ArXiv e-prints, arXiv:1803.07051

Milisavljevic, D., Margutti, R., Kamble, A., et al. 2015, ApJ, 815, 120

Modjaz, M., Blondin, S., Kirshner, R. P., et al. 2014, AJ, 147, 99

Moriya, T. J., Maeda, K., Taddia, F., et al. 2013, MNRAS, 435, 1520

Moriya, T. J., Nicholl, M., & Guillochon, J. 2018a, ArXiv e-prints, arXiv:1806.00090

Moriya, T. J., Sorokina, E. I., & Chevalier, R. A. 2018b, Space Sci. Rev., 214, 59

Nakamura, T., Mazzali, P. A., Nomoto, K., & Iwamoto, K. 2001, ApJ, 550, 991

Pastorello, A., Smartt, S. J., Botticella, M. T., et al. 2010, ApJL, 724, L16

Pastorello, A., Benetti, S., Brown, P. J., et al. 2015, MNRAS, 449, 1921

Patat, F., Cappellaro, E., Danziger, J., et al. 2001, ApJ, 555, 900

Perley, D. A., Chen, T.-W., Filippenko, A. V., Brink, T. G., & Zheng, W. 2017, The Astronomer's Telegram, 10587

Pettini, M., & Pagel, B. E. J. 2004, MNRAS, 348, L59

Poole, T. S., Breeveld, A. A., Page, M. J., et al. 2008, MNRAS, 383, 627

Quimby, R. M., Kulkarni, S. R., Kasliwal, M. M., et al. 2011, Nature, 474, 487

Schlafly, E. F., & Finkbeiner, D. P. 2011, ApJ, 737, 103

Smartt, S. J., Valenti, S., Fraser, M., et al. 2015, A&A, 579, A40

Smith, N., Silverman, J. M., Chornock, R., et al. 2009, ApJ, 695, 1334

Stritzinger, M., Taddia, F., Fransson, C., et al. 2012, ApJ, 756, 173

Taddia, F., Stritzinger, M. D., Sollerman, J., et al. 2013, A&A, 555, A10

Tonry, J. L., Denneau, L., Heinze, A. N., et al. 2018, PASP, 130, 064505

Valenti, S., Benetti, S., Cappellaro, E., et al. 2008, MNRAS, 383, 1485

Woosley, S. E. 2010, ApJL, 719, L204

—. 2017, ApJ, 836, 244

Yan, L., Quimby, R., Ofek, E., et al. 2015, ApJ, 814, 108

Yan, L., Lunnan, R., Perley, D. A., et al. 2017, ApJ, 848, 6

Yaron, O., & Gal-Yam, A. 2012, PASP, 124, 668

APPENDIX

One machine readable table: Pseudobolometric luminosity and photometry of SN 2017ens (UV through NIR). The magnitudes without uncertainties are 3σ detection limits. ATLAS *cyan* and *orange* bands are also converted to the SDSS system using our spectra (for prediscovery detection limits we adopt the first-epoch passband correction value).

Table 2:: Optical photometry of *griz* bands of SN 2017ens. The ">" denotes 3σ detection limits.

UT Date	MJD	Phase	*g* (error)	*r* (error)	*i* (error)	*z* (error)	Telescope/Instrument
2017 June 8	57912.992	-9.94	17.57 (0.05)	17.96 (0.05)	18.24 (0.04)	18.35 (0.06)	GROND
2017 June 10	57914.026	-9.01	17.53 (0.03)	17.89 (0.05)	18.16 (0.04)	18.28 (0.05)	GROND
2017 June 13	57917.011	-6.31	17.41 (0.08)	17.73 (0.04)	18.02 (0.06)	18.09 (0.06)	GROND
2017 June 20	57924.011	0.00	17.33 (0.06)	17.54 (0.04)	-	17.81 (0.06)	GROND
2017 June 25	57929.465	4.92	17.50 (0.04)	17.58 (0.03)	17.67 (0.05)	-	LCO
2017 June 29	57933.058	8.16	17.47 (0.01)	17.59 (0.02)	17.66 (0.06)	17.70 (0.03)	GROND
2017 July 2	57937.012	11.73	17.63 (0.04)	17.75 (0.07)	17.76 (0.06)	-	LCO
2017 July 3	57937.980	12.60	17.63 (0.07)	17.65 (0.06)	17.70 (0.07)	17.74 (0.06)	GROND
2017 July 3	57938.031	12.65	17.78 (0.05)	17.63 (0.05)	17.64 (0.06)	-	LCO
2017 July 4	57938.428	13.00	17.76 (0.08)	17.74 (0.07)	17.50 (0.08)	-	LCO
2017 July 7	57941.345	15.64	17.85 (0.06)	17.71 (0.06)	17.73 (0.05)	-	LCO
2017 July 7	57941.994	16.22	17.87 (0.04)	17.82 (0.04)	17.77 (0.04)	-	LCO
2017 July 10	57945.007	18.94	17.99 (0.03)	17.85 (0.03)	17.86 (0.04)	-	LCO
2017 July 12	57946.033	19.86	17.98 (0.03)	17.89 (0.05)	17.88 (0.05)	17.95 (0.04)	GROND
2017 July 14	57948.027	21.66	18.07 (0.09)	17.94 (0.03)	17.95 (0.04)	17.94 (0.07)	GROND
2017 July 14	57948.984	22.53	18.16 (0.07)	17.90 (0.06)	17.90 (0.06)	-	LCO
2017 July 16	57950.995	24.34	18.20 (0.01)	18.03 (0.03)	17.97 (0.06)	18.00 (0.05)	GROND
2017 July 19	57953.983	27.04	18.44 (0.07)	18.21 (0.06)	18.15 (0.10)	18.19 (0.04)	GROND
2017 July 20	57954.967	27.92	-	18.21 (0.08)	18.12 (0.10)	-	LCO
2017 July 21	57955.993	28.85	18.50 (0.05)	18.28 (0.05)	18.19 (0.06)	18.23 (0.03)	GROND
2017 July 24	57958.984	31.55	18.61 (0.05)	18.39 (0.05)	18.25 (0.05)	18.27 (0.04)	GROND
2017 July 27	57961.979	34.25	18.78 (0.04)	18.54 (0.05)	18.42 (0.06)	18.42 (0.05)	GROND
2017 July 31	57965.983	37.86	18.96 (0.06)	18.62 (0.06)	18.51 (0.07)	18.51 (0.06)	GROND
2017 August 1	57966.979	38.76	18.94 (0.04)	18.66 (0.05)	18.52 (0.06)	18.49 (0.05)	GROND
2017 August 9	57974.968	45.97	19.20 (0.05)	18.96 (0.23)	18.73 (0.07)	18.79 (0.07)	GROND
2017 December 16	58103.300	161.73	20.60 (0.05)	20.62 (0.05)	20.13 (0.07)	20.15 (0.10)	GROND
2017 December 22	58109.303	167.14	20.58 (0.05)	20.65 (0.06)	20.11 (0.07)	20.31 (0.09)	GROND
2017 December 27	58114.304	171.65	20.78 (0.06)	20.99 (0.05)	20.25 (0.06)	20.51 (0.06)	GROND
2018 January 4	58122.318	178.88	20.91 (0.08)	21.02 (0.06)	20.26 (0.08)	20.64 (0.07)	GROND
2018 January 6	58124.304	180.67	20.86 (0.06)	20.89 (0.07)	20.19 (0.05)	20.53 (0.07)	GROND
2018 January 12	58130.266	186.05	21.01 (0.06)	20.97 (0.06)	20.37 (0.10)	20.50 (0.06)	GROND
2018 January 15	58133.263	188.75	20.80 (0.05)	20.83 (0.05)	20.26 (0.06)	20.41 (0.06)	GROND
2018 January 18	58136.303	191.50	20.91 (0.08)	20.96 (0.05)	20.31 (0.08)	20.58 (0.05)	GROND
2018 January 22	58140.283	195.09	20.84 (0.07)	20.98 (0.04)	20.33 (0.09)	20.61 (0.06)	GROND
2018 January 24	58142.282	196.89	20.82 (0.06)	20.92 (0.05)	20.27 (0.08)	20.53 (0.06)	GROND
2018 January 27	58145.319	199.63	20.98 (0.06)	21.10 (0.05)	20.36 (0.09)	20.73 (0.06)	GROND
2018 February 1	58150.333	204.15	20.92 (0.17)	21.26 (0.14)	20.63 (0.13)	20.63 (0.16)	GROND
2018 February 12	58161.258	214.01	21.04 (0.05)	20.94 (0.04)	20.28 (0.09)	20.61 (0.08)	GROND
2018 February 20	58169.268	221.23	20.93 (0.05)	21.01 (0.05)	20.34 (0.08)	20.63 (0.07)	GROND
2018 February 27	58176.338	227.61	20.96 (0.08)	21 (0.04)	20.3 (0.05)	20.83 (0.05)	GROND
2018 March 19	58196.179	245.51	21.23 (0.08)	21.37 (0.05)	20.47 (0.09)	21.01 (0.06)	GROND
2018 March 25	58202.285	251.01	21.05 (0.07)	21.23 (0.06)	20.36 (0.09)	20.79 (0.07)	GROND
2018 April 6	58214.119	261.69	21.05 (0.05)	21.11 (0.06)	20.41 (0.09)	20.66 (0.08)	GROND
2018 April 18	58226.095	272.49	21.07 (0.07)	21.02 (0.04)	20.26 (0.05)	20.72 (0.09)	GROND

Table 3:: Optical photometry of SN 2017ens in ATLAS *cyan* and *orange* bands.[a]

UT Date	MJD	Phase	c (error)	o (error)	c → g	o → r
2017 May 10	57883.428	-36.61	-	> 19.03	-	> 19.08
2017 May 10	57883.443	-36.59	-	> 19.13	-	> 19.18
2017 May 10	57883.459	-36.58	-	> 18.89	-	> 18.94
2017 May 10	57883.478	-36.56	-	> 18.76	-	> 18.81
2017 May 11	57884.365	-35.76	-	> 19.58	-	> 19.63
2017 May 11	57884.401	-35.73	-	> 19.35	-	> 19.4
2017 May 11	57884.416	-35.72	-	> 19.32	-	> 19.37
2017 May 13	57886.285	-34.03	-	> 19.69	-	> 19.74
2017 May 13	57886.299	-34.02	-	> 19.66	-	> 19.71
2017 May 13	57886.314	-34.00	-	> 19.53	-	> 19.58
2017 May 13	57886.328	-33.99	-	> 19.53	-	> 19.58
2017 May 19	57892.370	-28.54	-	> 20.31	-	> 20.36
2017 May 19	57892.399	-28.52	-	> 20.23	-	> 20.28
2017 May 19	57892.427	-28.49	-	> 20.25	-	> 20.3
2017 May 20	57893.299	-27.70	-	> 20.22	-	> 20.27
2017 May 20	57893.317	-27.69	-	> 20.18	-	> 20.23
2017 May 20	57893.350	-27.66	-	> 19.70	-	> 19.75
2017 May 23	57896.373	-24.93	> 20.06	-	> 20.00	-
2017 May 24	57897.289	-24.10	-	> 20.06	-	> 20.11
2018 May 24	57897.306	-24.09	-	> 20.03	-	> 20.08
2019 May 24	57897.323	-24.07	-	> 20.06	-	> 20.11
2017 May 24	57897.340	-24.06	-	> 20.14	-	> 20.19
2017 May 25	57898.332	-23.16	-	> 20.18	-	> 20.23
2017 May 27	57900.346	-24.93	> 20.36	-	> 20.30	-
2017 May 27	57900.381	-24.32	> 20.34	-	> 20.28	-
2017 May 27	57900.416	-24.28	> 20.35	-	> 20.29	-
2017 May 29	57902.268	-19.61	-	> 20.29	-	> 20.34
2017 May 29	57902.301	-19.58	-	> 20.12	-	> 20.17
2017 May 29	57902.318	-19.57	-	> 20.13	-	> 20.18
2017 May 31	57904.286	-17.79	> 19.65	-	> 19.59	-
2017 June 1	57905.257	-16.92	-	> 19.81	-	> 19.86
2017 June 1	57905.271	-16.90	-	> 19.66	-	> 19.71
2017 June 2	57906.257	-16.01	-	> 19.40	-	> 19.45
2017 June 4	57908.326	-14.15	-	> 17.81	-	> 17.86
2017 June 4	57908.394	-14.09	-	> 17.88	-	> 17.93
2017 June 5	57909.274	-13.29	-	18.62 ± 0.12	-	18.67
2017 June 6	57910.275	-12.39	-	18.6 ± 0.10	-	18.65
2017 June 9	57913.276	-9.68	-	18.08 ± 0.10	-	18.13
2017 June 10	57914.267	-8.79	-	17.86 ± 0.08	-	17.91
2017 June 12	57916.327	-6.93	-	17.94 ± 0.05	-	17.99
2017 June 15	57919.320	-4.23	-	17.78 ± 0.06	-	17.83
2017 June 16	57920.316	-3.33	-	17.68 ± 0.02	-	17.73
2017 June 19	57923.327	-0.62	-	17.69 ± 0.16	-	17.74
2017 June 20	57924.303	0.26	-	17.57 ± 0.04	-	17.62
2017 June 23	57927.304	2.97	-	17.62 ± 0.03	-	17.67
2017 June 23	57927.322	2.99	-	17.64 ± 0.05	-	17.69
2017 June 27	57931.297	6.57	-	17.56 ± 0.03	-	17.61
2017 July 5	57939.275	13.77	-	17.67 ± 0.06	-	17.77
2017 July 8	57942.273	16.47	-	17.78 ± 0.07	-	17.88
2017 July 9	57943.255	17.36	-	17.75 ± 0.08	-	17.85
2017 July 10	57944.261	18.27	-	17.81 ± 0.06	-	17.91
2017 July 11	57945.263	19.17	-	17.9 ± 0.04	-	18.00
2017 July 15	57949.261	22.78	-	17.96 ± 0.05	-	18.06
2017 July 17	57951.260	24.58	-	18.09 ± 0.05	-	18.29
2017 July 21	57955.258	28.19	-	18.26 ± 0.08	-	18.46

[a]We also convert these to the SDSS system using our spectra.
For prediscovery detection limits we adopt the first-epoch S-correction value.

Table 4:: Optical photometry of SN 2017ens using Lulin SLT telescope.

UT Date	MJD	Phase	B	V	R	I
2017 June 23	57927.572	3.21	17.55 (0.15)	17.36 (0.19)	17.30 (0.25)	17.27 (0.26)
2017 June 26	57930.551	5.90	17.77 (0.13)	17.36 (0.25)	17.29 (0.35)	17.07 (0.30)

Table 5:: Ultraviolet photometry of SN 2017ens in the *Swift* UVOT bands.

UT Date	MJD	Phase	v	b	u	$uvw1$	$uvm2$	$uvw2$
2017 June 28	57932	7.21	17.58 (0.15)	17.59 (0.09)	17.91 (0.08)	18.48 (0.07)	18.72 (0.06)	18.96 (0.08)
2017 July 3	57937	11.72	17.50 (0.16)	17.88 (0.11)	18.00 (0.09)	18.78 (0.09)	19.01 (0.07)	19.20 (0.08)
2017 July 25	57959	31.56	18.85 (0.37)	18.85 (0.18)	19.13 (0.13)	20.10 (0.13)	20.33 (0.10)	20.53 (0.11)
2018 January 22	58140	194.83	-	-	-	> 21.85	> 22.61	22.36 (0.26)
2018 January 30	58150	203.85	-	-	21.18 (0.13)	-	-	22.42 (0.21)

Table 6:: NIR photometry of SN 2017ens in the GROND NIR bands.

UT Date	MJD	Phase	J	H	K_s
2017 June 8	57912.992	-9.94	18.80 (0.12)	19.14 (0.19)	> 19.52
2017 June 10	57914.026	-9.01	18.82 (0.11)	19.31 (0.18)	> 19.20
2017 June 13	57917.011	-6.31	18.52 (0.10)	18.89 (0.13)	19.18 (0.27)
2017 June 20	57924.011	0.00	18.38 (0.10)	18.59 (0.13)	-
2017 June 29	57933.058	8.16	18.18 (0.11)	18.52 (0.14)	18.64 (0.20)
2017 July 3	57937.980	12.60	18.16 (0.16)	18.31 (0.20)	-
2017 July 12	57946.033	19.86	18.37 (0.10)	18.61 (0.15)	18.85 (0.21)
2017 July 14	57948.027	21.66	18.19 (0.12)	18.66 (0.18)	> 18.85
2017 July 16	57950.995	24.34	18.48 (0.15)	18.83 (0.26)	> 18.93
2017 July 19	57953.983	27.04	18.42 (0.12)	18.89 (0.14)	19.10 (0.24)
2017 July 21	57955.993	28.85	18.52 (0.10)	18.74 (0.14)	19.10 (0.18)
2017 July 24	57958.984	31.55	18.63 (0.10)	19.10 (0.19)	> 19.42
2017 July 27	57961.979	34.25	18.70 (0.11)	19.06 (0.16)	> 19.48
2017 July 31	57965.983	37.86	18.79 (0.16)	> 19.51	> 19.29
2017 August 1	57966.979	38.76	18.87 (0.18)	> 19.47	> 19.26
2017 August 9	57974.968	45.97	19.02 (0.26)	> 19.18	-
2017 December 16	58103.300	161.73	> 20.91	19.64 (0.21)	> 19.59
2017 December 22	58109.303	167.14	20.03 (0.18)	> 20.37	-
2017 December 27	58114.304	171.65	20.42 (0.15)	20.47 (0.20)	19.86 (0.23)
2018 January 4	58122.318	178.88	20.42 (0.21)	20.30 (0.26)	> 19.82
2018 January 6	58124.304	180.67	20.35 (0.15)	20.72 (0.28)	19.76 (0.26)
2018 January 12	58130.266	186.05	20.77 (0.22)	19.93 (0.18)	-
2018 January 15	58133.263	188.75	20.35 (0.17)	20.18 (0.21)	19.73 (0.22)
2018 January 18	58136.303	191.50	20.34 (0.16)	20.20 (0.21)	-
2018 January 22	58140.283	195.09	20.33 (0.17)	20.35 (0.25)	19.95 (0.30)
2018 January 24	58142.282	196.89	20.63 (0.23)	20.24 (0.25)	19.60 (0.24)
2018 January 27	58145.319	199.63	20.49 (0.18)	20.18 (0.18)	> 19.60
2018 February 1	58150.333	204.15	> 20.53	> 20.26	> 18.97
2018 February 12	58161.258	214.01	20.43 (0.14)	20.24 (0.17)	> 19.85
2018 February 18	58167.310	219.46	20.39 (0.17)	20.48 (0.24)	> 19.82
2018 February 20	58169.268	221.23	20.57 (0.24)	> 20.70	> 19.93
2018 February 27	58176.338	227.61	20.32 (0.15)	20.58 (0.22)	19.52 (0.26)
2018 March 7	58184.248	234.74	20.43 (0.19)	20.39 (0.24)	> 19.981
2018 March 19	58196.179	245.51	20.46 (0.16)	20.25 (0.17)	19.63 (0.24)
2018 March 25	58202.285	251.01	20.53 (0.18)	20.43 (0.23)	> 19.92
2018 April 6	58214.119	261.69	20.66 (0.24)	20.53 (0.32)	> 19.99
2018 April 18	58226.095	272.49	> 21.07	> 20.61	> 19.44

Table 7:: Pseudobolometric luminosity of SN 2017ens
(UV through NIR).

Phase (day)	$\log L_{\rm bol}$ ($\rm erg\,s^{-1}$)	Phase (day)	$\log L_{\rm bol}$ ($\rm erg\,s^{-1}$)
-13.30	43.45 ± 0.08	19.86	43.61 ± 0.01
-12.39	43.45 ± 0.08	21.66	43.59 ± 0.01
-9.94	43.65 ± 0.01	22.53	43.58 ± 0.01
-9.69	43.65 ± 0.01	22.78	43.57 ± 0.01
-9.01	43.67 ± 0.01	24.34	43.55 ± 0.01
-8.80	43.68 ± 0.01	24.58	43.54 ± 0.01
-6.94	43.70 ± 0.01	27.04	43.48 ± 0.01
-6.31	43.73 ± 0.01	27.92	43.47 ± 0.01
-4.23	43.74 ± 0.01	28.18	43.47 ± 0.02
-3.34	43.75 ± 0.01	28.85	43.46 ± 0.02
-0.62	43.77 ± 0.01	31.55	43.42 ± 0.02
0.00	43.78 ± 0.01	34.25	43.36 ± 0.02
0.26	43.78 ± 0.01	37.86	43.31 ± 0.02
2.97	43.76 ± 0.01	38.76	43.31 ± 0.02
4.92	43.76 ± 0.01	45.97	43.23 ± 0.03
6.57	43.77 ± 0.01	161.73	42.65 ± 0.03
8.16	43.76 ± 0.00	167.14	42.69 ± 0.03
11.73	43.71 ± 0.01	171.65	42.56 ± 0.03
12.60	43.71 ± 0.01	178.88	42.53 ± 0.03
12.65	43.69 ± 0.01	180.67	42.56 ± 0.03
13.00	43.70 ± 0.01	186.05	42.54 ± 0.03
13.76	43.69 ± 0.01	188.75	42.59 ± 0.03
15.64	43.66 ± 0.01	191.50	42.56 ± 0.04
16.22	43.65 ± 0.01	195.09	42.54 ± 0.04
16.47	43.65 ± 0.01	196.89	42.54 ± 0.04
17.35	43.65 ± 0.01	199.63	42.50 ± 0.04
18.27	43.64 ± 0.01	204.15	42.49 ± 0.05
18.94	43.62 ± 0.01	214.01	42.52 ± 0.04
19.17	43.62 ± 0.01	221.23	42.52 ± 0.04